Biophysical Journal
Article

Biophysical Society

FSCS Reveals the Complexity of Lipid Domain Dynamics in the Plasma Membrane of Live Cells

Philip R. Nicovich,[1,2,3,*] Joanna M. Kwiatek,[1,2] Yuanqing Ma,[1,2] Aleš Benda,[4] and Katharina Gaus[1,2]
[1]EMBL Australia Node in Single Molecule Science, School of Medical Sciences, and [2]ARC Centre of Excellence in Advanced Molecular Imaging, University of New South Wales, Sydney, New South Wales, Australia; [3]Allen Institute for Brain Science, Seattle, Washington; and [4]Imaging Methods Core Facility at BIOCEV, Faculty of Sciences, Charles University, Vestec, Czech Republic

ABSTRACT The coexistence of lipid domains with different degrees of lipid packing in the plasma membrane of mammalian cells has been postulated, but direct evidence has so far been challenging to obtain because of the small size and short lifetime of these domains in live cells. Here, we use fluorescence spectral correlation spectroscopy in conjunction with a probe sensitive to the membrane environment to quantify spectral fluctuations associated with dynamics of membrane domains in live cells. With this method, we show that membrane domains are present in live COS-7 cells and have a lifetime lower bound of 5.90 and 14.69 ms for the ordered and disordered phases, respectively. Comparisons to simulations indicate that the underlying mechanism of these fluctuations is complex but qualitatively described by a combination of dye diffusion between membrane domains as well as the motion of domains within the membrane.

INTRODUCTION

The biophysical properties of the cell plasma membrane are thought to arise from the diversity of lipids and their interactions. For example, the lipid raft hypothesis suggests that membrane heterogeneity is caused by the associations of saturated phospholipids such as sphingomyelin with cholesterol to form a highly ordered lipid domain that diffuses in a sea of less ordered and more fluid phospholipids (1,2). Further, the hypothesis postulates that a distinct subset of membrane proteins partition preferentially in the raft-like lipid environments, affecting protein clustering, interactions, and diffusion dynamics. An alternative theory is the picket-fence model, which proposes that the plasma membrane is segregated into compartments by underlying cortical actin filaments that are associated with the membrane (3). In this model, membrane lipids and proteins exhibit random diffusion within the compartments but require hop diffusion to cross the membrane-actin barriers. Other studies have proposed that glycosylphosphatidylinositol-anchored proteins are directly coupled to cortical actin in an ATP-dependent manner, resulting in the formation of cholesterol-enriched nanoclusters (4,5). It should be noted that these models do not exclude each other so that different organizing principles could yield coexisting membrane domains within the plasma membrane (6).

We and others have previously used environment-sensitive fluorescent probes such as Laurdan, di-4-ANEPPDHQ, and NR12S (7–9), to visualize differences in membrane order in intact and living cells (10,11). For example, we showed that the plasma membrane at T cell activation sites (12) and focal adhesions (13,14) is more ordered than the unstimulated regions in the same cell and that membrane condensation contributes to the formation of clathrin-independent endocytic invagination (15–17). Environment-sensitive fluorescent probes have the advantage that they are often only fluorescent in the hydrophobic environment of the membrane (i.e., minimal background fluorescence from the aqueous media), are not required to partition preferentially into a particular lipid phase, and report the biophysical state of the membrane via spectral shifts or intensity changes. For example, the membrane-order-sensitive dye NR12S displays a large blue shift in the emission maxima in liquid-ordered (L_o) lipid vesicles composed of sphingomyelin and cholesterol compared to liquid-disordered (L_d) vesicles composed of 1,2-dioleoyl-sn-glycero-3-phosphocholine (DOPC) (8). This probe inserts itself exclusively into the outer leaflet of both model and cell membranes, avoiding issues with internalization and labeling of internal membranes (8). In phase-separated liposomes, NR12S exhibits no preference for L_o or L_d phases (8).

Submitted July 7, 2017, and accepted for publication April 10, 2018.

*Correspondence: rustyn@alleninstitute.org

Philip R. Nicovich and Joanna M. Kwiatek contributed equally to this work.

Editor: Joseph Falke.

https://doi.org/10.1016/j.bpj.2018.04.050

© 2018 Biophysical Society.

This is an open access article under the CC BY-NC-ND license (http://creativecommons.org/licenses/by-nc-nd/4.0/).

Because individual membrane domains in cell membranes cannot be resolved with diffraction-limited microscopy (18,19), most of our biophysical understanding of lipid phase separation and phase coexistence comes from model membranes (20–22). Researchers have used various techniques to map the phase diagrams of ternary lipid mixtures (23) and four-component bilayers (24) and observed cholesterol-rich L_o-like nanodomains of ~10 nm in one-component lipid membranes and DOPC-sphingomyelin mixtures with high cholesterol content (21,22). In an attempt to provide evidence of L_o-like nanodomains in cell membranes that are below the resolution limit of conventional microscopes, we previously unmixed the fluorescence lifetime signal from Laurdan membranes (19). We found that the plasma membrane is better described as a mixture of two lipid environments of low and high membrane order than as a single membrane environment of intermediate order (19). Interestingly, the oxysterol 7-ketocholesterol (7KC), which increases the overall fluidity of the membrane (25), reduced the relative abundance of the ordered membrane but retained the coexistence of two distinct membrane environments (19). Other aspects of lipid phase separation, such as the fluctuations near the critical point, have so far only been observed in model membranes (26,27).

A technique that has the required temporal resolution to detect even short-lived membrane domains is fluorescence correlation spectroscopy (FCS). By performing FCS measurements at different spatial scales (variable-spot FCS), Wawrezinieck et al. established the so-called FCS diffusion law, in which spot size is plotted against diffusion time through the spot size (28). The FCS diffusion law can distinguish between free diffusion and diffusion impacted by confinement in domains and membrane compartments. Superresolution techniques, such as stimulated emission depletion, dramatically improve the resolution of FCS (29) and reveal the confinement times of different lipids. For example, fluorescently labeled phosphoethanolamine, a putative nonraft lipid, diffused across the detection spot in ~1 ms, whereas sphingomyelin or raft-associated glycosylphosphatidylinositol-anchored proteins took ~10 ms (30,31) and appeared to be trapped in domains of ~20 nm in diameter (31).

In this article, we combined the high temporal resolution of FCS with the environmentally sensitive probe NR12S in a spectral unmixing approach called fluorescence spectral correlation spectroscopy (FSCS) (32). When FSCS is applied to environment-sensitive fluorescent probes such as NR12S, the fluorescence emitted from more ordered and more fluid membranes can be distinguished by spectral channels. The subsequent analysis essentially treats signals from the separate environments as separate emissive species. This yields timescales of NR12S signal fluctuations originating from the two lipid environments independently. FSCS is analogous to fluorescence lifetime correlation spectroscopy (33,34), in which the fluorescence lifetime is used to segregate fluorescent signals with overlapping spectra so that correlation curves can be calculated for different signals. FSCS too can separate simultaneous signals arising from multiple fluorophores with overlapping spectra (32). FSCS has the advantage that recording spectra with multiple spectrally resolved detectors is technically simpler than using lifetime measurements and can utilize dyes that show a spectral, but not lifetime, shift in response to the environment, which is the case with NR12S. We applied FSCS to NR12S-stained live cells and found evidence for two coexisting lipid environments, even in cells that have been treated with an oxysterol, 7KC, that increases the overall fluidity of cell membranes. To understand the origin of the fluorescence fluctuation arising from these domains and their dynamic coexistence, we performed a series of simulations and qualitatively compared them to the experimental FSCS data.

METHODS

Lipid vesicles were formed by extrusion of the desired lipid mixture (Lo, 70:30 n-palmitoyl-sphingomyelin:cholesterol; Ld 80:20 DOPC:cholesterol; Avanti Polar Lipids, Alabaster, AL) through 100 nm pores at 55°C. Supported lipid bilayers (SLBs) were prepared by diluting extruded and stained vesicles in Ca^{2+} buffer (10 mM HEPES, 150 mM NaCl, 1 mM $CaCl_2$ (pH 7.4)) and incubated on glass coverslips for 30 min. The formed bilayer was gently flushed three times with HEPES buffer (pH 7.4) to remove remaining vesicles. Samples were stained with NR12S (N-[3-[[9-(diethylamino)-5-oxo-5H-benzo[α]phenoxazin-2-yl]oxy]-propyl-N-methyl-N-(3-sulfopropyl)-1-dodecanaminium; obtained from Dr. Andrey Klymchenko) at a concentration of 0.7 μM for 15 min at room temperature.

COS-7 live cells were stained with NR12S by adding dye solution to the growth medium at a final concentration of 105 nM for 30 min at 37°C. Where indicated, cells were additionally treated with 30 μM oxysterol 7KC (C6970-000; Steraloids, Newport, RI) complexed to 38 mM methyl-β-cyclodextrin (C4555; Sigma, St. Louis, MO) at a concentration of 30 μM simultaneously with the NR12S staining. Cells were treated with latrunculin B (LatB) (L5288; Sigma) by adding LatB to the growth medium at a concentration of 5 μM in the final 5 min of NR12S staining. Cells were then washed three times with phosphate-buffered saline and imaged in Dulbecco's modified eagle medium.

Data were acquired on a Zeiss LSM 780 confocal microscope using a C-Apochromat 40× 1.20 NA water-immersion objective with 514 nm excitation (7 μW at objective back aperture). Emission was separated by a dichroic mirror and emission filter before passing through a 36.3 μm pinhole. The emission signal was split by a prism before reaching a 32-channel gallium arsenide phosphide photodetector operating in single-photon counting mode. The detector signal was binned into six spectral channels with centers/bandwidths of 552.9/35.6, 579.6/17.8, 597.4/17.8, 615.2/17.8, 637.5/26.7, and 673.1/44.5 nm, respectively. These ranges yield more even count rates across the spectral channels than are obtained from channels with equal spectral widths. The proper z-position of the focus during the acquisition of single point data was confirmed by subsequent line scan FCS acquisition, which provides the actual illuminated area radius.

Spectral analysis and correlations were calculated using home-written LabVIEW and MATLAB (The MathWorks, Natick, MA) code, including an implementation of the multi-τ algorithm for correlation of time-tagged single photon counting data, which accepted double-precision weights for each photon based on the spectra of the two emissive species (see Supporting Materials and Methods).

Fluorophores (n = 200) were simulated as noninteracting particles experiencing two-dimensional Brownian motion within the simulated area (5 × 5 μm) with periodic boundary conditions. The magnitude of motion of the particle between time step $t - 1$ to t was defined by the identity of the particle, assigned as existing in either the L_o or L_d state. This identity was either assigned at the beginning of the simulation and not varied (the "independent" simulation condition) or evaluated at each time step. In these cases, the particle identity was assigned based on the particle's location within a two-dimensional (2D) binary domain-containing lattice ("static domains" or "motile domains") or by a two-state hidden Markov simulation ("switching domains"). The particle identity of L_o was assigned a value equal to 1 and the identity of L_d was assigned a value of 0. Cross talk was introduced by biasing these binary values toward the mean of 0.5, either by a multiplicative factor (in the "independent" case) or by blurring the binary lattice with a Gaussian spatial filter.

The domain-containing lattice was generated as a partially relaxed binary 2D Ising spin lattice in which the input temperature and number of relaxation cycles were used to generate domains of various sizes (here, interaction strength = k_B; temperature = 50, 0.5, 0.01, or 0.001 K for small (1.1 ± 0.05 pixels), medium (25.9 ± 0.51 pixels), and large domains (49.6 ± 1.8 pixels); either 50 (small and medium domains) or 100 (large domains) relaxation iterations). These domain sizes were evaluated through pair correlation and approximation of the resulting curve with a Gaussian domain model (fullwidth at half-maximum values are reported). This Ising lattice was simulated at a 1 nm pixel size with total dimensions of 2 × 2 μm placed at the center of the particle simulation area. The remainder of the area was filled with randomly assigned binary values. In the "static domains" case, this lattice was held fixed and only the particles diffused; in the "motile domains" case, the lattice was also allowed to diffuse randomly within the 2D field. This was accomplished by simulating a single diffusing particle of a defined diffusion constant and shifting the position of all diffusing particles by this position when determining the particle identity at that time step.

Diffusion constants were set at 0.1 $\mu m^2/s$ for the L_o phase and 0.3 $\mu m^2/s$ for the L_d phase (35) for the data presented here in the "independent," "static domain," "eroded," or "blended" cases (Fig. 2; Figs. S6–S8). These values give a reasonable qualitative match to the experimental data under the simulation conditions and fall within an order of magnitude of diffusion constants found in other works (36). In the "motile domain" case (Fig. 3 *A*), the domains were given a diffusion constant of 5.0 $\mu m^2/s$ and probes diffusion constants of 0 $\mu m^2/s$. For the "switching domains" case (Fig. 3 *C*), the switching rate was set to 5 s^{-1} for the $L_o \rightarrow L_d$ transition and 15 s^{-1} for the $L_d \rightarrow L_o$ rate, and both L_o and L_d diffusion constants were set to 0.01 $\mu m^2/s$ (setting these diffusion constants to 0 $\mu m^2/s$ produced anomalous results). When combining both domain and particle diffusion (Fig. 4), these diffusion constants were set to 0.05, 0.3, and 0.1 $\mu m^2/s$ for the domain, L_o particle, and L_d particle diffusion, respectively.

Simulations were prerun for 10,000 time steps of 1 ms to allow the system to approach the steady state. The simulation was then recorded for an additional 10,000 time steps (10 s). The generated position of each particle was then converted into intensity within the simulated focal spot by evaluating a Gaussian of defined width ($1/e^2$ radius of 230 nm) and centered in the simulation box at each particle's position. This intensity was multiplied either by the particle's identity or by 1 minus the particle's identity to generate L_o- and L_d-specific intensity traces. Matrix multiplication of each of these traces by the respective L_o and L_d reference spectra generated identity-specific spectral intensity traces, the sum of which represented the simulated six-channel intensity trace for the simulation. This, along with the generating reference spectra, was passed to an unmixing and correlation function (via fast Fourier transform) to generate the resulting simulated auto- and cross correlation curves. Twenty runs of each simulation were accumulated, and averages for each of the correlation curves were generated before plotting.

Statistical analysis was performed where indicated using the two-sample *t*-test using the provided MATLAB function ttest2.

Analysis and simulation codes are available through the author's GitHub repository (https://github.com/PRNicovich/FSCS.git).

RESULTS AND DISCUSSION

FSCS in live cells with the polarity-sensitive membrane dye NR12S

In FSCS, the fluorescence intensity of NR12S emitted from live cells is spectrally split or "unmixed" into "ordered" and "fluid" membranes with 16 μs temporal resolution (Fig. S1). It is assumed that the observed spectra originate from at least two fluorescent species that coexist within the observation volume (~200 nm in diameter) at any given time. The linear spectral unmixing calculation (28) reconstitutes the contributions from a given number of species to the overall spectra. This is done with so-called filter coefficients that are applied to the total mixed spectrum on a per photon basis. This generates the contributions of a signal photon in a given spectral channel at a given time to one of the decomposed signals. It is this decomposition that allows retention of the dynamics to generate the correlation curves.

In our study, we assume the coexistence of only two NR12S species: one residing in "L_o" membranes and the other in "L_d" membranes. Please note that this assumption only allows us to address whether membrane domains of different orders dynamically coexist in cells; it does not allow us to draw conclusions about the similarity or difference between these two membrane environments. Thus, we could use model membranes as reference data that represent membranes in L_o and L_d environments that are vastly different from each other. The use of such simple model systems does not presume that the "L_o" and "L_d" membranes unmixed from our experimental data are indeed L_o and L_d environments; the two cellular membrane environments could be much more similar in their degree of membrane order than the two reference model systems. To ensure that the brightness and diffusion constant of the environmentally sensitive dye has no impact on the FSCS auto- and cross correlation curves, we conducted simulations (Fig. S6) that illustrate the suitability of NR12S as a probe in our work. Additional semiempirical modeling indicates that the chosen reference spectra drawn from model membrane systems are at or near the optimum basis spectra to describe the experimentally observed NR12S emission spectra (Supporting Materials and Methods and Fig. S8).

We recorded spectra and intensity fluctuations of NR12S-labeled COS-7 cells and in model membranes in six spectral channels with 16 μs temporal resolution. Autocorrelations from the fluctuation of NR12S signal as it transited through the detection volume centered on SLBs, which are characteristic of the L_o phase, showed an average diffusion time of 3.55 ± 0.79 ms (± SD, n = 8, Fig. S1) using a 2D free diffusion model. Within this model environment, we can

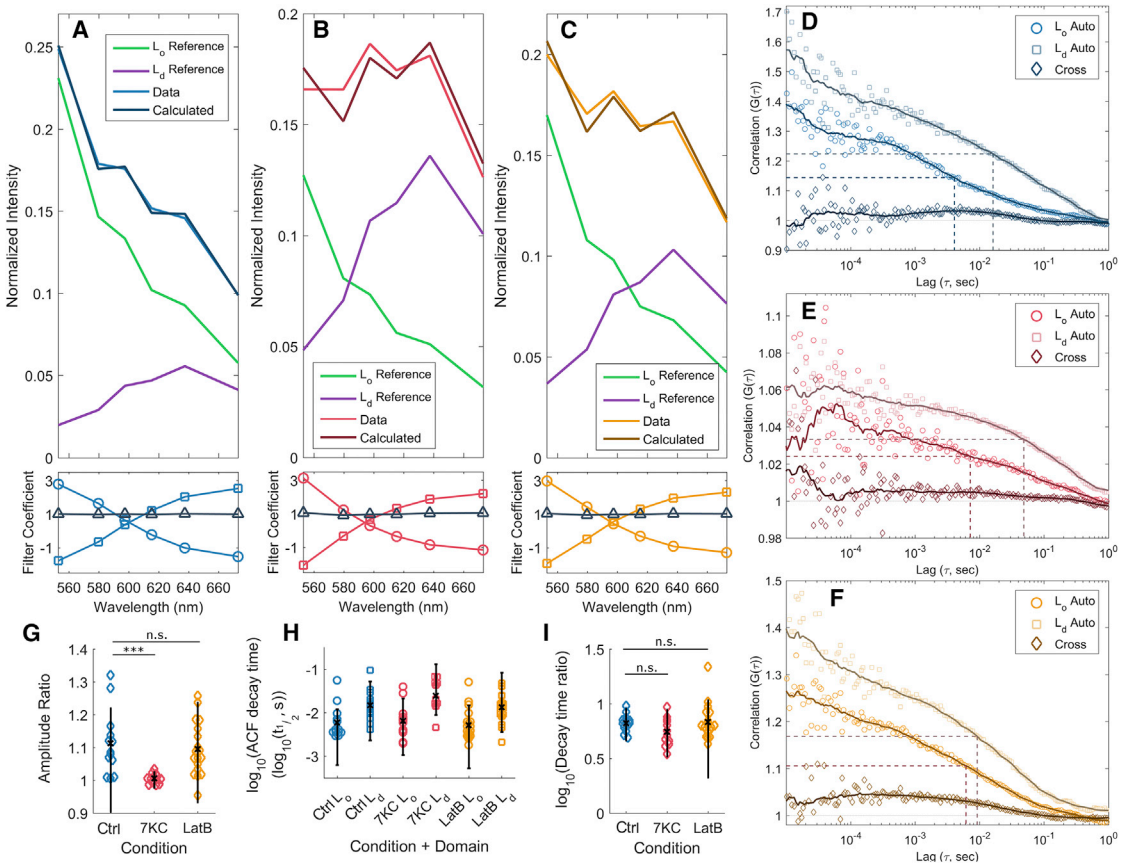

FIGURE 1 FSCS in live COS-7 cells. (*A–C*) Representative measured and fitted spectra of NR12S in control (*A*), 7KC-treated (*B*), and LatB-treated (*C*) cells are shown as well as reference data from model membranes in L_o (*green*) and L_d (*purple*) phases. NR12S was excited at 514 nm, and emission was collected in channels with centers/bandwidths of 552.9/35.6, 579.6/17.8, 597.4/17.8, 615.2/17.8, 637.5/26.7, and 673.1/44.5 nm, respectively. Using the reference data from the model membranes, filter coefficients (*A–C*, *bottom*) were calculated so that the cellular spectra could be described as a two-component system (calculated, *top*). Filter coefficients (*bottom*) represent the relative weighting for each channel for the L_o (*circles*) and L_d (*squares*) spectra, with sums that should equal unity (*triangles*). Data are representative of at least 12 independent measurements. (*D–F*) Representative correlations for control (*D*), 7KC-treated (*E*), and LatB-treated (*F*) cells were calculated by applying extracted filter coefficients as in (*A*)–(*C*) to yield autocorrelations for the L_o (*circle*) and L_d (*square*) components of the cellular data and the corresponding cross correlation (*diamonds*). Dashed lines indicate autocorrelation decay timescales ($t_{1/2}$ values). (*G*) Ratio of autocorrelation amplitudes is shown. (*G*) A summary of autocorrelation decay timescales is shown. (*I*) Ratio of autocorrelation decay times is shown. In (*G*)–(*I*), each colored symbol is one measurement (n = 13, 12, and 19 for control, 7KC, and LatB conditions, respectively) with mean (*black cross*) and error bars (*black lines*) corresponding to 5–95% confidence interval. ***$p \leq 0.001$ by two-sample *t*-test. To see this figure in color, go online.

assume that dye motion is the only cause of fluorescence fluctuations on the 10^{-4}–10^{0} s timescale.

The spectrum acquired from NR12S in these SLB experiments was used as the reference for the pure L_o environment. A similar measurement was performed in single-phase vesicles characteristic of the L_d phase (Figs. 1, *A–C* and S1). Spectra obtained in cells could be then decomposed into a linear combination of these reference spectra, producing a scaled sum spectrum that reasonably matched the original observed spectrum. Furthermore, the decomposition of the observed spectrum into scaled reference spectra provided FSCS filter coefficients for each of the six spectral channels.

That the sum of filter coefficients at each spectral channel did not significantly deviate from unity further indicates that the observed spectrum could be adequately described by two components (Fig. 1, *A–C*, *bottom*). This does not contradict the presence of "in between" membrane environments or those in which the dye exhibits behavior indicative of an environment somewhere between the extremes of the L_o and L_d reference environments; rather, it shows that a linear combination of these two environments is sufficient to explain the observed behavior.

Untreated cells showed a preference for the ordered phase and enrichment with 7KC, which acts as a spacer in the membrane, greatly increasing the contribution of the disordered phase (19) (Fig. 1 *B*). LatB treatment, which depolymerizes actin, shows a similar enhancement of the disordered phase in the bulk spectrum but to a lesser extent than 7KC treatment (Fig. 1 *C*).

These filter coefficients were applied to the measured photon arrival stream to produce the FSCS curves for the

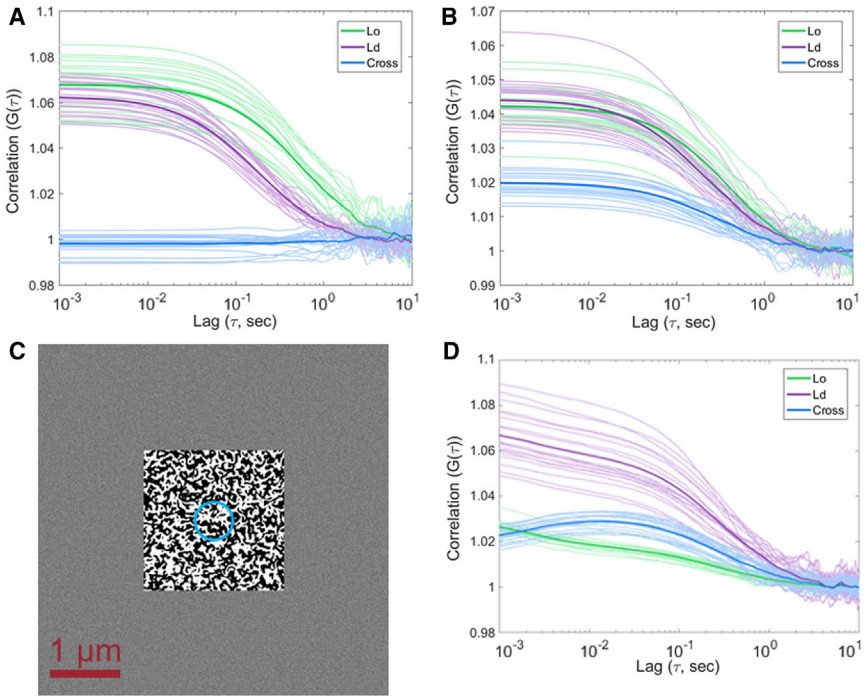

FIGURE 2 Simulations of freely diffusing probes in static modeled membranes. (*A*) Correlations are shown from simulations in which the diffusion rate of the probe differs by environment, but the probes do not change spectral identity after the initial assignment. (*B*) Correlations from the same simulations are shown, but now with cross talk between spectral channels. (*C*) A heterogeneous 2D membrane environment is simulated as a 2×2 μm semirelaxed binary Ising lattice within a 5×5 μm box. The $1/e^2$ diameter of the simulated Gaussian focal spot is shown in blue. (*D*) Correlations from simulations in which probes are allowed to diffuse and probe identity at a given time is determined by the lattice identity at the probe's location. Data are processed as for experimental FSCS data sets, resulting in autocorrelation curves shown in (*A*), (*B*), and (*D*) for the L_o (*green*) and L_d (*purple*) components and their cross correlation curves (*blue*) under the respective simulation conditions. To see this figure in color, go online.

two observed spectral components, corresponding to the L_o and L_d contributions. Representative correlation results appear in Fig. 1, *D–F*, with all measured correlation curves appearing in Figs. S2–S4.

Autocorrelation FSCS curves have a total amplitude approximately equal to the inverse of the average number of molecules in the focal volume. Within this amplitude, the respective curves are divided proportionally to the intensity of the signal from a given NR12S spectral signal and the square of the diffusing entity brightness. The resulting FSCS autocorrelations in live cells show that NR12S in the L_d phase resulted in a stronger correlation signal than in the L_o phase across all conditions (Fig. 1 *G*). The ratio of amplitudes between L_d and L_o autocorrelations was reduced under 7KC treatment ($p = 0.0010$) but did not significantly vary under LatB treatment ($p = 0.59$, Fig. 1 *G*). This could represent a difference in prevalence of a given membrane environment, of the probe's preference for one environment over the other, or of a change in diffusing entity brightness in each environment.

All autocorrelation curves show a decrease from a maximum near zero lag ($\tau = 0$) to a value close to 1 signifying no correlation at times approaching $\tau = \infty$, as is typical for aperiodic motion of probes through a single focal volume. The intervening curve shape is complex and not readily fitted to a multicomponent 2D or three-dimensional diffusion model. To compare timescales, the model-free half-amplitude autocorrelation decay time ($t_{1/2}$) was used. For cases of single-component 2D diffusion, this value is equal to the diffusion time (τ_D), but for more complex (or unknown) sources of fluorescence fluctuations, it provides a means to compare timescales without fitting to an explicit model.

Mean decay lifetimes were 5.90, 6.48, and 5.15 ms for the L_o component and 14.69, 24.38, and 13.13 ms for the L_d component in control, 7KC-treated, and LatB-treated cells, respectively (Fig. 1 *H*; Table S1). Previous work indicated that lipid molecules are trapped or confined on timescales of 10–11 ms (31,37); our results show similar timescales are associated with changes in lipid environment for the probe and that each environment is associated with a distinct timescale.

Autocorrelation decay times showed a similar trend to the amplitude results wherein the L_d autocorrelation decayed to the half amplitude point in a longer time than the L_o phase. This trend carried across treatments, whereas the difference in autocorrelation decay times between the two phases did not vary significantly with treatment ($p = 0.075$ for 7KC, $p = 0.50$ for LatB) (Fig. 1 *I*). As the autocorrelation times are longer than diffusion times observed within SLBs (3.55 ± 0.79 ms in L_d model membranes vs. 13.13–24.37 ms for the L_d component in live cells, $\pm$SD), this means that the diffusion in cell membranes was greatly hindered to constrain the dye molecules within a region smaller than the focal volume. Such constrained motion is a known feature of molecules in plasma membranes; the cause is attributed to multiscale confinement of the lipids to regions 20–750 nm in size (31,37).

Weighting detected photons with filters for the two spectral components respectively further allows the calculation

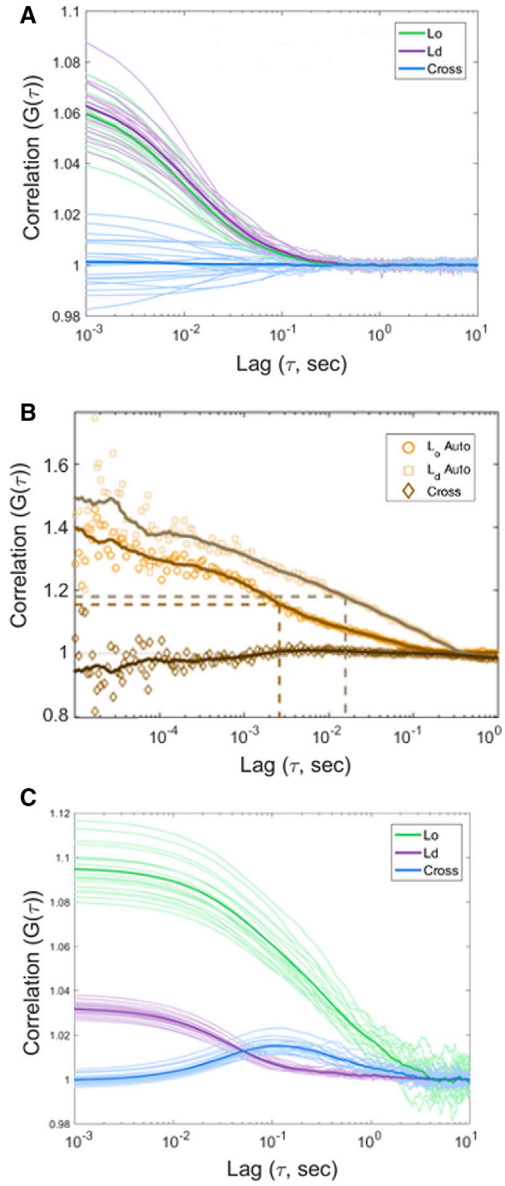

FIGURE 3 Simulation results from dynamic domain environments. (*A*) Correlations from simulations in which dyes are fixed relative to the lattice are shown, but the lattice and probes diffuse through the static observational volume. (*B*) A representative result from LatB-treated cells shows anticorrelation behavior at short timescales (for experimental details, see Fig. 1). Dashed lines indicate the $t_{1/2}$ timescales. (*C*) Correlations from simulations in which probes are additionally allowed to slowly diffuse in addition to switching identities are shown via a hidden Markov model. In (*B*) and (*C*), autocorrelation curves for the L_o (*green*) and L_d (*purple*) components and cross correlation curves (*blue*) are shown. To see this figure in color, go online.

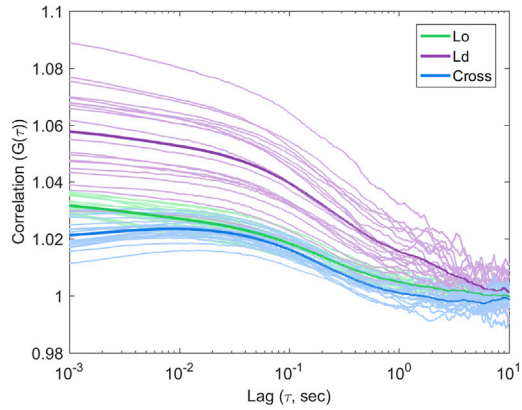

FIGURE 4 Correlation results from simulations with simultaneous probe diffusion through the modeled domain lattice and diffusion of the underlying domain lattice relative to the observational volume. Autocorrelation curves for the L_o (*green*) and L_d (*purple*) components and cross correlation curves (*blue*) are shown. To see this figure in color, go online.

of an FSCS cross correlation curve. This curve represents the timescale and magnitude of similarities (or dissimilarities) in the fluctuations between the two spectral channels. Representative cross correlations appear in the correlation curves in Fig. 1, *D–F*, with the full set of measured correlations in Figs. S2–S4. As with the autocorrelation curves, the observed cross correlation signals are complex and not readily fitted to an a priori model of membrane behavior. Still, it is possible to describe commonalities observed in the results.

In all cases, observed cross correlations were of lower amplitude than were the autocorrelations. A common motif in the cross correlation curve is a peak occurring at or near the timescale of the autocorrelation decays (see Fig. 1 *D*). Such a peak was observed in 11/13 control cells, 4/12 7KC-treated cells, and 9/19 LatB-treated cells over the timescale of the autocorrelation decays (10^{-4}–10^{-1} s). These peaks were at timescales comparable to the L_o and L_d autocorrelation decays in the control cell case (Fig. S2), and where present, this moves to faster timescales when cells were treated with 7KC or LatB (Figs. S3 and S4). The reduction in cross correlation peak timescale upon treatment is consistent with a reduction in domain size or reduction in confinement strength of the dye within a single domain.

Other cross correlation curves show anticorrelation (values below 1) at short timescales ($\tau < 10^{-4}$ s). This feature is observed in 2/13 control cells, 0/12 7KC-treated cells, and 5/19 of the LatB-treated cells. An additional 5/19 cells showed persistent anti-cross-correlation at all measured (10^{-5}–10^{0} s) timescales.

Simulations of NR12S fluctuations in a heterogeneous membrane environment

Three mechanisms are proposed to potentially give rise to the observed fluorescence fluctuations: 1) the transit of probe through a static, if heterogeneous, membrane; 2) the transit of membrane domains relative to the focal volume; and 3) fluctuation of domain order identity in each location in the membrane. The true process could be a combination of all three hypothesized mechanisms, but the FSCS signal will be dominated by the fastest process, which yields a

change in intensity of a single probe species with other processes occurring at longer timescales and lower magnitudes masked.

Simulations provide a means to investigate the implications of these proposed mechanisms on the observable auto- and cross correlation curves. These simulations assume a heterogeneous 2D membrane of a binary mixture of L_o and L_d domains, generated as a semirelaxed Ising lattice. This model is a reasonable approximation of observed membrane behavior on the nanometer scale (26,38). The degree of relaxation (and resulting size of membrane domains) is held as a variable, as is the membrane viscosity within each environment, degree of motion of the domains, and other potential transition rates. The focal volume is matched to the experimental point-spread function (approximated as a Gaussian with width $\sigma = 230$ nm) and centered in a much larger simulated area (5×5 μm). Dye intensity is assumed to be equal in both environments. Dye abundance is held constant at 8 dyes/μm^2 in the simulated membrane, and L_o and L_d spectra are those measured experimentally. Simulations were run 20 times in each condition for 10^5 ms in 1 ms steps, and the correlation curves were averaged.

As a control, dyes were assigned an environmental and corresponding spectral identity at the start of the simulation and allowed to diffuse. These simulations are not sufficient to yield the observed correlation behavior (Fig. 2). Without switching of dye spectral identity, there is no significant average cross correlation signal, and individual simulation runs show small deviations around 1 that do not change with timescale (Fig. 2 *A*). Introducing cross talk between channels does add a cross correlation decay as essentially a scaled replica of the average autocorrelation curves (Fig. 2 *B*; Fig. S5). Importantly, this curve does not show a peak but rather a monotonic decay. These results show that dye switching spectral identity is required for the observed auto- and cross correlation signals. It is not sufficient to have two populations of dye that do not alter their spectral properties through the course of the experiment to recapitulate the experimental observations.

If instead the dyes diffuse within a heterogeneous environment, many of the features are observed in the experimental results (Fig. 2, *C* and *D*). Here, a binary membrane lattice domain environment with equal proportion of the two environments was generated, and dyes were allowed to diffuse within this environment. The spectral identity of a given dye was assigned by the value of the binary lattice at the dye's position at that time point. An additional parameter was added to allow the dye diffusion rate to vary along with the lattice environment. The simulation progressed for 10^4 time steps to relax to a steady state before the recording of the simulated fluorescence output began.

These simulations produce two key features in the experimental correlations. First, the autocorrelation curves show a deviation in amplitude along with timescale. In all cases with equal probe intensity and domain abundance, the faster diffusional component shows a lower amplitude and faster decay timescale than the slower diffusional component. This occurs even with the two membrane environments being present in equal amounts and without any thermodynamic effects on the preference of the probe for a given environment. The difference in amplitude points to kinetic trapping within an environment of higher effective viscosity as a possible mechanism for the observed difference in autocorrelation amplitude. The observed autocorrelation curves nearly always have the ordered phase autocorrelation curve at higher amplitude, which, given that this phase is of higher viscosity, is consistent with this explanation.

The cross correlation curves under these conditions are also qualitatively consistent with the broad peak near the autocorrelation decay timescale observed in the experimental data. This peak is present in all simulated data sets and represents the motion of dye from one membrane environment to another. The peak position varies linearly with simulated domain size, being at a longer timescale for larger domains. Here, an increase in simulated domain size from 25.93 ± 0.51 nm ($\pm$SD, n = 120) to 49.61 ± 1.78 nm ($\pm$SD, n = 40) results in an increase in the peak position from 12.15 ± 3.4 ms ($\pm$SD) to 25.5 ± 5.0 ms ($\pm$SD). If domain size is exceedingly small, approaching the 1 nm pixel size of the simulated area, then three identical correlation curves are observed. Together, these results indicate that the domains must be on the same size scale but smaller than the focal spot for the observed experimental behavior. If they are too small, then the differential correlation behavior is not observed, whereas if they are too large, the domains would be visible in diffraction-limited imaging. Ultimately, previous work indicating a domain size of tens of nanometers (19,31) is consistent with the observations here.

Kinetic trapping as the primary mechanism for autocorrelation amplitude differences assumes that the two phases are present in near-equal amounts. Manipulating the prevalence of environments in the lattice additionally alters this difference in autocorrelation amplitude, with the ratio of autocorrelation amplitudes being switched when the prevalence of the faster diffusional environment is sufficient to overcome the kinetic trapping effects (Fig. S6). For simulated probes with diffusion constants of 0.1 and 0.3 μm^2/s for the L_o and L_d phases, respectively, this crossover occurs when the abundance of the L_d domain increases from 50% to between 44% (Fig. S6, *A* and *B*) and 31% (Fig. S6, *C* and *D*). In these trials, the cross correlation always shows a peak at a timescale approximately equal to the autocorrelation decays and with an amplitude between the two autocorrelation curves at the peak position. The experimental data are qualitatively consistent with a near-equal distribution of domain abundance.

Intensity differences between probes in the L_o or L_d environment have an additional compounding effect. It has been previously shown that NR12S can vary by a factor of ~2 in

fluorescence quantum yield based on the polarizability of the surrounding environment (8). We ran simulations in equivalent environments while varying the diffusion constant and relative intensity of the probe in different environments (Fig. S7). The autocorrelation amplitude did vary with probe brightness; an increase in brightness yielded an increase in autocorrelation amplitude for that phase.

The effect of different diffusion coefficients in the two phases worked in concert with the brightness effect on autocorrelation amplitude. In the experimental data, we observe that the autocorrelation in the ordered channel is always at a longer timescale than in the fluid channel. All experimental systems show an autocorrelation amplitude ratio of the fluid to the ordered phase greater than 1 (Fig. 1 *G*). We expect the fluid channel autocorrelation to have a greater amplitude than the ordered channel autocorrelation, given equal probe brightness.

Varying the simulated probe brightness by a factor of two away from equal is sufficient to reach the crossover point such that the brighter ordered channel shows greater autocorrelation amplitude than the dimmer fluid phase (simulated diffusion constants of 0.3 and 0.1 μm2/s and relative brightness of 2:1 for the ordered and fluid environment, respectively). The converse brightness ratio with the same diffusion constants yields simulated amplitudes in the proper sign but with ordered/fluid autocorrelation amplitudes greater than most of the observed experimental data. Although it is difficult to extract an experimental diffusion constant given the complex membrane environment, these data together suggest that the relative brightness of the NR12S probe in the experimental membrane environments is within a factor of 2 or equivalent.

Introducing an intermediate membrane environment state (one between the binary L_o or L_d extreme) by blurring the binary lattice does not alter the qualitative features of the correlation curves (Fig. S8). Modeling domain boundaries as gradients rather than as discrete binary transitions resulted in correlation curves that retained the qualitative features of the curves from the binary condition. The only effect is a reduction in contrast between the three correlation curves with reduced discrete binary character. As with the spectral data, it is not possible to discern if there are truly two distinct membrane environments in the experimental data or if a continuum of environments exists between the two extremes. However, the data observed requires membrane heterogeneity and is not inconsistent with a binary lattice of two distinct membrane states. Additionally, this loss of correlation contrast may provide a route to experimentally quantify the level of discrete character in the membrane, especially if this can be varied by temperature or drug treatment.

Together, these coupled effects of domain abundance, size, and viscosity in the membrane environment on the correlation curves are challenging to disentangle. However, the qualitative features of the correlation curves remain consistent. As such, it is reasonable to continue to compare simulated results against the experimental data to determine parameters that describe the qualitative correlation features observed. From these, we can determine that the experimental behavior is consistent with membrane domains in near-equal abundance with approximately discrete transitions while differing in viscosity. Further, the NR12S probe brightness in the two environments is nearly equivalent.

Simulating mobile domains and domain formation and disassembly

On their own, the cross correlation curves from these simulations are in good agreement with many of the cross correlation curves in the experimental data. However, the experimental data do not always show the same peak as that in the simulations, but in some cases, no peak or a negative anticorrelation signal is shown. Additionally, the cross correlation curve is always at a lower amplitude than both autocorrelation curves rather than crossing the lower-amplitude autocorrelation curve, as seen in these simulations. Whereas this simulated mechanism does explain much of the data, it is not sufficient to explain all qualitative features.

Rather than holding the domain lattice position constant and allowing probes to move, the probes can be held static relative to the lattice while the lattice is allowed to move as a single unit (Fig. 3 *A*). This would represent a case in which domains moving through a cell membrane carry relatively fixed membrane constituents along with them. Under these conditions, no difference in autocorrelation amplitude or timescale is seen between the two spectral components. The cross correlation curve, however, can recapitulate the observed anticorrelation behavior seen in many of the experimental data sets. This anticorrelation would represent a case in which the presence of one environment excludes the signal from the other being present. In previous work, this was observed with a mixed population of vesicles, each of either L_o or L_d environment, in which the size of the vesicle was sufficient to exclude others from the focal volume (32). Here, the mosaic of the domain lattice accomplishes the same effect.

Anti-cross-correlation behavior was primarily observed in the LatB condition (Fig. 3 *B*), suggesting the role of the actin meshwork in domain formation and diffusion confinement within the membrane (37,39). Removal of this confinement through actin depolymerization could yield more motile domains and subsequently the observed correlation behavior.

Notably, the conditions that can yield this anti-cross-correlation are also likely to yield positive cross correlation of the same amplitude and timescale across the measurement window (Fig. 3 *A*). Such variability in cross correlation in the simulated results helps explain the variability observed in the experimental results, especially under LatB treatment conditions.

A change in domain identity around the dye molecules is the third possibility. Such behavior could be attributed to that of a membrane at or near its critical temperature. Emergent from these conditions are domains similar to the Ising-like regions invoked above but with domain identity at a given point evolving over time as domains percolate within the membrane environment (38,40). Simulations for this mechanism modeled each dye using a hidden Markov model switching between L_o and L_d identity at a specified rate. There was no spatial connection between simulated probe molecules, but this should not affect the results, as switching entire domains would be equivalent to switching individual probes at the probe densities characteristic of these experiments.

Allowing for both probe identity switching and diffusion (slower than that in the diffusion-only case), it was possible to observe some general parallels between the simulated and observed curves (Fig. 3 *C*). Interestingly, without additionally allowing for diffusion of the probe, the autocorrelation results for both phases were identical, with the cross correlation being equal in opposite magnitude regardless of specified switching timescale. Like with the diffusion-only case, the autocorrelation curve amplitudes diverge with the longer-lived state, resulting in a greater amplitude. A peak in the cross correlation is observed at a similar timescale to that of the autocorrelation decay. However, the shape of this peak differs from that observed in the diffusion-only case. Rather than a broad peak with positive signal at $\tau = 0$ and increasing to a maximum, the peak here is very close to 1 (uncorrelated) at $\tau = 0$ and rises to a relatively sharp peak at the maximal value. The former diffusion-only peak shape is a much closer fit to the experimental cross correlation curves than that generated by Markov switching of dye identity.

It remains that no one mechanism simulated is sufficient to describe the observed correlation curves. Dye diffusion through a heterogeneous membrane can capture the difference in autocorrelation amplitudes and the shape and presence of the common cross correlation peak motif. Membrane domain translation alternatively can explain the anti-cross-correlation seen in the experimental data. Although a single mechanism may be a simpler explanation, it is fully possible that a more complex set of mechanisms underlies the behavior of probe molecules in the cell membrane.

Combining mechanisms of dye molecules diffusing in and out of mobile domains

To test one such set of combination of mechanisms, we allowed both dye diffusion in and out of domains and lattice motion during the simulation. The result yielded a set of curves well-approximating much of the experimental data (Fig. 4). The amplitude of the correlation curves is correct, with the autocorrelation of the slower-diffusing environment yielding the greatest amplitude, followed by the autocorrelation of the slower environment and finally the cross correlation curve. The cross correlation curve maintains the broad peak with a positive signal at $\tau = 0$.

The match between these simulations and the observed data implies that the dynamics in the cell membrane environment is complex and not well described by a single mechanism. Two separate and plausible mechanisms operating on similar timescales describe the experimental data better (Fig. 4) than any single simulated mechanism alone (Fig. 3). It is therefore likely that multiple mechanisms are involved, and any experiment biased to show only one is present in driving membrane dynamics may well be confirmed. These results show that care should be taken in the interpretation of these results to not unduly exclude other mechanisms. The ability of FSCS does allow for extra information in the form of the cross correlation that is not present in conventional FCS. These crossing events prove exceptionally useful in distinguishing between possible mechanisms, enforcing the utility of this approach to investigate lipid dynamics in live cells.

CONCLUSIONS

We demonstrate that FSCS is an appropriate tool for monitoring the dynamics of an environmentally sensitive lipid probe within a dynamic membrane environment. Mechanisms underlying the fluorescence fluctuations are proposed, and we find no single mechanism is sufficient to describe the observed fluctuations; at minimum, a combination of two mechanisms—probe motion through distinct membrane domain environments and motion of domains through the membrane—is necessary to qualitatively recapitulate the correlation behavior observed.

Regardless of mechanism, these experiments show that domains must exist as distinct environments to yield the observed spectrally separable dye signals. Further, these environments are likely to exist on the length scale of tens of nanometers and persist for at least the timescale of the autocorrelation decay i.e., 5.90 and 14.69 ms for the ordered and disordered phases, respectively (Fig. 1 *G*). These results confirm the presence of distinct lipid phases in live cells and that these domains can fluctuate on biologically relevant timescales.

SUPPORTING MATERIAL

Supporting Materials and Methods, nine figures, and one table are available at http://www.biophysj.org/biophysj/supplemental/S0006-3495(18)30588-5.

AUTHOR CONTRIBUTIONS

J.M.K. and A.B. designed and performed the experiments and initial analysis. P.R.N. performed the analysis and simulation, wrote the manuscript, and generated the figures. K.G. conceived the study and wrote the manuscript. Y.M. contributed to the manuscript preparation.

ACKNOWLEGEMENTS

The authors gratefully acknowledge Andrey Klymchenko and Yves Mély for their provision of the NR12S dye essential for this work.

K.G. and P.R.N. acknowledge funding from the Australian Research Council Centre of Excellence in Advanced Molecular Imaging (CE140100011 to K.G.), Australian Research Council (LP140100967 to K.G. and P.R.N. and DP130100269 to K.G.), and National Health and Medical Research Council of Australia (1059278 to K.G.). A.B. acknowledges the support from CZ.02.1.01/0.0/0.0/16_013/0001775 funded by the Ministry of Education, Youth and Sports, Czech Republic. J.M.K. and Y.M. each acknowledge University International Postgraduate Awards from the University of New South Wales, Australia.

REFERENCES

1. Simons, K., and D. Toomre. 2000. Lipid rafts and signal transduction. *Nat. Rev. Mol. Cell Biol.* 1:31–39.
2. Simons, K., and E. Ikonen. 1997. Functional rafts in cell membranes. *Nature.* 387:569–572.
3. Kusumi, A., H. Ike, …, T. Fujiwara. 2005. Single-molecule tracking of membrane molecules: plasma membrane compartmentalization and dynamic assembly of raft-philic signaling molecules. *Semin. Immunol.* 17:3–21.
4. Goswami, D., K. Gowrishankar, …, S. Mayor. 2008. Nanoclusters of GPI-anchored proteins are formed by cortical actin-driven activity. *Cell.* 135:1085–1097.
5. Gowrishankar, K., S. Ghosh, …, M. Rao. 2012. Active remodeling of cortical actin regulates spatiotemporal organization of cell surface molecules. *Cell.* 149:1353–1367.
6. Carquin, M., L. D'Auria, …, D. Tyteca. 2016. Recent progress on lipid lateral heterogeneity in plasma membranes: from rafts to submicrometric domains. *Prog. Lipid Res.* 62:1–24.
7. Dietrich, C., L. A. Bagatolli, …, E. Gratton. 2001. Lipid rafts reconstituted in model membranes. *Biophys. J.* 80:1417–1428.
8. Kucherak, O. A., S. Oncul, …, A. S. Klymchenko. 2010. Switchable nile red-based probe for cholesterol and lipid order at the outer leaflet of biomembranes. *J. Am. Chem. Soc.* 132:4907–4916.
9. Jin, L., A. C. Millard, …, L. M. Loew. 2006. Characterization and application of a new optical probe for membrane lipid domains. *Biophys. J.* 90:2563–2575.
10. Owen, D. M., C. Rentero, …, K. Gaus. 2011. Quantitative imaging of membrane lipid order in cells and organisms. *Nat. Protoc.* 7:24–35.
11. Gaus, K., T. Zech, and T. Harder. 2006. Visualizing membrane microdomains by Laurdan 2-photon microscopy. *Mol. Membr. Biol.* 23:41–48.
12. Gaus, K., E. Chklovskaia, …, T. Harder. 2005. Condensation of the plasma membrane at the site of T lymphocyte activation. *J. Cell Biol.* 171:121–131.
13. Gaus, K., S. Le Lay, …, M. A. Schwartz. 2006. Integrin-mediated adhesion regulates membrane order. *J. Cell Biol.* 174:725–734.
14. Le Saux, G., A. Magenau, …, K. Gaus. 2011. Spacing of integrin ligands influences signal transduction in endothelial cells. *Biophys. J.* 101:764–773.
15. Römer, W., L. Berland, …, L. Johannes. 2007. Shiga toxin induces tubular membrane invaginations for its uptake into cells. *Nature.* 450:670–675.
16. Römer, W., L. L. Pontani, …, L. Johannes. 2010. Actin dynamics drive membrane reorganization and scission in clathrin-independent endocytosis. *Cell.* 140:540–553.
17. Lakshminarayan, R., C. Wunder, …, L. Johannes. 2014. Galectin-3 drives glycosphingolipid-dependent biogenesis of clathrin-independent carriers. *Nat. Cell Biol.* 16:595–606.
18. Owen, D. M., and K. Gaus. 2013. Imaging lipid domains in cell membranes: the advent of super-resolution fluorescence microscopy. *Front. Plant Sci.* 4:503.
19. Owen, D. M., D. J. Williamson, …, K. Gaus. 2012. Sub-resolution lipid domains exist in the plasma membrane and regulate protein diffusion and distribution. *Nat. Commun.* 3:1256.
20. McIntosh, T. J. 2015. Stepping between membrane microdomains. *Biophys. J.* 108:783–784.
21. Koukalová, A., M. Amaro, …, R. Šachl. 2017. Lipid driven nanodomains in giant lipid vesicles are fluid and disordered. *Sci. Rep.* 7:5460.
22. Armstrong, C. L., D. Marquardt, …, M. C. Rheinstädter. 2013. The observation of highly ordered domains in membranes with cholesterol. *PLoS One.* 8:e66162.
23. Bezlyepkina, N., R. S. Gracià, …, R. Dimova. 2013. Phase diagram and tie-line determination for the ternary mixture DOPC/eSM/cholesterol. *Biophys. J.* 104:1456–1464.
24. Goh, S. L., J. J. Amazon, and G. W. Feigenson. 2013. Toward a better raft model: modulated phases in the four-component bilayer, DSPC/DOPC/POPC/CHOL. *Biophys. J.* 104:853–862.
25. Rentero, C., T. Zech, …, K. Gaus. 2008. Functional implications of plasma membrane condensation for T cell activation. *PLoS One.* 3:e2262.
26. Nielsen, L. K., T. Bjørnholm, and O. G. Mouritsen. 2000. Fluctuations caught in the act. *Nature.* 404:352.
27. Veatch, S. L., P. Cicuta, …, B. Baird. 2008. Critical fluctuations in plasma membrane vesicles. *ACS Chem. Biol.* 3:287–293.
28. Wawrezinieck, L., H. Rigneault, …, P. F. Lenne. 2005. Fluorescence correlation spectroscopy diffusion laws to probe the submicron cell membrane organization. *Biophys. J.* 89:4029–4042.
29. Ruprecht, V., S. Wieser, …, G. J. Schütz. 2011. Spot variation fluorescence correlation spectroscopy allows for superresolution chronoscopy of confinement times in membranes. *Biophys. J.* 100:2839–2845.
30. Honigmann, A., V. Mueller, …, C. Eggeling. 2014. Scanning STED-FCS reveals spatiotemporal heterogeneity of lipid interaction in the plasma membrane of living cells. *Nat. Commun.* 5:5412.
31. Eggeling, C., C. Ringemann, …, S. W. Hell. 2009. Direct observation of the nanoscale dynamics of membrane lipids in a living cell. *Nature.* 457:1159–1162.
32. Benda, A., P. Kapusta, …, K. Gaus. 2014. Fluorescence spectral correlation spectroscopy (FSCS) for probes with highly overlapping emission spectra. *Opt. Express.* 22:2973–2988.
33. Böhmer, M., M. Wahl, …, J. Enderlein. 2002. Time-resolved fluorescence correlation spectroscopy. *Chem. Phys. Lett.* 353:439–445.
34. Kapusta, P., R. Macháň, …, M. Hof. 2012. Fluorescence lifetime correlation spectroscopy (FLCS): concepts, applications and outlook. *Int. J. Mol. Sci.* 13:12890–12910.
35. Knight, J. D., M. G. Lerner, …, J. J. Falke. 2010. Single molecule diffusion of membrane-bound proteins: window into lipid contacts and bilayer dynamics. *Biophys. J.* 99:2879–2887.
36. Lagerholm, B. C., D. M. Andrade, …, C. Eggeling. 2017. Convergence of lateral dynamic measurements in the plasma membrane of live cells from single particle tracking and STED-FCS. *J. Phys. D Appl. Phys.* 50:063001.
37. Fujiwara, T., K. Ritchie, …, A. Kusumi. 2002. Phospholipids undergo hop diffusion in compartmentalized cell membrane. *J. Cell Biol.* 157:1071–1081.
38. Machta, B. B., S. Papanikolaou, …, S. L. Veatch. 2011. Minimal model of plasma membrane heterogeneity requires coupling cortical actin to criticality. *Biophys. J.* 100:1668–1677.
39. Trimble, W. S., and S. Grinstein. 2015. Barriers to the free diffusion of proteins and lipids in the plasma membrane. *J. Cell Biol.* 208:259–271.
40. Burns, M. C., M. Nouri, and S. L. Veatch. 2016. Spot size variation FCS in simulations of the 2D Ising model. *J. Phys. D Appl. Phys.* 49:214001.

Biophysical Journal, Volume *114*

Supplemental Information

FSCS Reveals the Complexity of Lipid Domain Dynamics in the Plasma Membrane of Live Cells

Philip R. Nicovich, Joanna M. Kwiatek, Yuanqing Ma, Aleš Benda, and Katharina Gaus

Supplemental Information for: Lifetime of Cellular Membrane Domains Measured by Fluorescence Spectral Correlation Spectroscopy

Philip R Nicovich[*,1,2,3], Joanna M. Kwiatek[*,1,2], Yuanqing Ma[1,2], Aleš Benda[2,3] and Katharina Gaus[1,2]

[1] *EMBL Australia Node in Single Molecule Science, School of Medical Sciences, University of New South Wales, Sydney, Australia.*
[2] *ARC Centre of Excellence in Advanced Molecular Imaging, University of New South Wales, Sydney, Australia*
[3] *Allen Institute for Brain Science, Seattle, Washington, USA*
[4] *Imaging methods core facility at BIOCEV, Faculty of Sciences, Charles University, Průmyslová 595, 252 42 Vestec, Czech Republic*
[*] *These authors shared equally in this work*

FSCS Theory

As presented in (*1*), the principle of FSCS relies on the fact that the spectrum of a mixture of N multiple emissive species at any time t can be described as a linearly-weighted combination of the spectra of the constituent species. This holds true across a given number of j spectral channels, such that

$$I_j(t) = \sum_{i=1}^{N} w_{i,j}(t) p_{i,j}(t) \tag{1}$$

where $I_j(t)$, $w_{i,j}(t)$, and $p_{i,j}(t)$ are the total intensity, weighting coefficient of component i, and pure spectrum of component i, all at time t and in spectral channel j. Given that the number of spectral channels exceeds the number of emissive species and the photon distribution remains Poissonian, single-value decomposition can be applied and Eq 1 can be re-written in terms of the total intensity, weighting coefficient, and a filter coefficient $f_{j,k}(t)$ for spectral channel j and component k.

$$w_k(t) = \sum_{j=1}^{M} f_{j,k}(t) I_j(t) \tag{2}$$

This weighting coefficient $w_k(t)$ here is the more familiar single scalar value result used in spectral unmixing for discerning contributions of separate emitters in spectral confocal imaging or other spectral decomposition techniques.

A matrix of filter coefficients $F(i,j) = f_{j,k}$ can be calculated from straightforward matrix operations given area-normalized spectral for the spectra of each emissive component and the spectrum to be decomposed.

$$F = ([P]^T diag\langle I(t)\rangle_t^{-1})[P])^{-1} [P]^T diag\langle I(t)\rangle_t^{-1} \tag{3}$$

where $P(i,j) = p_{i,j}$, or the area-normalized spectral intensity of pure component i in spectral channel j.

Photons arrivals during the FSCS acquisition are recorded with both the timestamp and the spectral channel in which the photon was detected. A weighting coefficient vector $w_k(t)$ for each constituent component is generated by treating matrix F as a look-up table returning the associated filter coefficient $f_{j,k}$ for channel j and component k. The correlation as a function of lag time τ between the signals from components k and l is then defined as

$$G_{k,l}(\tau) = \frac{\langle w_k(t)\, w_l(t+\tau)\rangle_t}{\langle w_k(t)\rangle_t \langle w_l(t)\rangle_t} \tag{4}$$

where $k = l$ in the case of autocorrelation and $k \neq l$ for cross-correlation. Efficiently calculating correlations can be accomplished through the method described by Wahl (*2*), but where the weight of each photon is given by $w_k(t)$ rather than the usual value of 1 (*3*).

Here each measurement of 180 seconds was split equally into ten time intervals and autocorrelations calculated for each with equal weighting for all spectral channels ($w = 1$ for each photon). The K time segments (here $K = 6$) which correlations most closely matched the mean correlation (assessed as sum of squares difference) were carried forward. The auto- and cross-correlations for those K time segments were then evaluated given the spectral weighting values for the channel in which each photon was detected.

Given the complex diffusion mechanisms anticipated for the samples under study, it is necessary to define a method for timescale analysis that is not dependent on a particular diffusional model. As used in previous work, the $t_{1/2}$ value, or the time for the correlation to decay to half its value at 0 time is appropriate (*1*, *4*). Given the noise in the correlation at short timescales, we substitute the value of the correlation at a range of short lag (τ) values for the value at $\tau = 0$. For data presented in Figure S1 this is the mean value of the correlation at $1x10^{-4} < \tau \leq 5x10^{-4}$ seconds and in Figure 1 $5x10^{-4} < \tau < 5x10^{-3}$ seconds. We point out that for the case of simple two-dimensional diffusion of the form $G(\tau) = (1 + \frac{t}{\tau_D})^{-1}$, one can trivially derive that $t_{1/2} = \tau_D$. Taking into account triplet transitions yields the expression

$$t_{1/2} = \tau_T\, W(z) - 2T\,\tau_D + \tau_D \tag{5a}$$

$$z = 2T\frac{\tau_D}{\tau_T} exp\left[\frac{(2T-1)\tau_D}{\tau_T}\right] \tag{5b}$$

where T is the triplet fraction, τ_T the triplet timescale, and W the Lambert W function. Extending this to three-dimensional diffusion with or without including triplet states becomes quite complex and beyond the scope required here. This expression demonstrates that the value for $t_{1/2}$ is a weighted average of the timescales present in the experiment.

With this estimate for the diffusion timescale τ_D we can use the Stokes-Einstein relationship (6) to yield parameters of the experimental system. Here

$$\frac{\omega_{xy}^{o2}}{4\tau_D} = D = \frac{k_b T}{6\pi\,\eta\,R_h} \tag{6}$$

where k_b is the Boltzmann constant, T temperature, η the environment viscosity, and R_h the radius of hydration of the diffusing species. We estimate the lateral beam waist as $\omega_{xy}^{o2} = \lambda/(1.22\,n\,NA)$ where λ is the excitation wavelength (514 nm), n the refractive index of the medium (1.33) and NA the numerical aperture of the system (1.20). Here this relationship is used in validating model membrane viscosity where the diffusional environment is sufficiently uncomplicated such that the approximation $t_{1/2} \approx \tau_D$ is appropriate. In other cases the value of $t_{1/2}$ is used as a comparison between conditions and not fit to a diffusion model.

Probe distribution and brightness within L_o and L_d environments

Previous work established that NR12S in phase-separated GUVs shows similar preference for the Lo and Ld phases (*5*). It was noted that this behavior is uncommon amongst environmentally-sensitive dyes enhancing the choice of NR12S as a selected probe for these experiments. However the exact preference for one phase versus the other is difficult to establish based on fluorescence intensity alone as the quantum yield of the NR12S fluorophore can vary by nearly a factor of 2 based on the polarizability of the surrounding lipid solvent.

To address the effect on the FSCS results of a possible difference in probe affinity and fluorescence efficiency in different lipid environments we performed additional simulations. In these simulations we kept the probe density and diffusional mode constant, but varied the intensity of the individual probes based on the surrounding environment. At the same time we varied the diffusion constant of the probe within the two membrane environments.

Simulations show that a difference in diffusion constant between the two membrane phases is sufficient to produce a difference in both autocorrelation time and amplitude (manuscript Figure 2D). This occurs with equal abundance of the two simulated phases as well as no environmentally-sensitive difference in probe brightness. In this situation the phase showing a greater value for the simulated diffusion constant will have a lower amplitude than the phase with the lesser value for diffusion constant. In other words, the phase with faster diffusion will have a lower amplitude in the corresponding autocorrelation function given equal phase abundance and probe brightness.

At the same time, it is possible for probe brightness to influence the autocorrelation amplitude. Increasing probe brightness in a given phase relative to the other correspondingly increases the autocorrelation amplitude for that phase.

From the experimental data we observe the Ld phase always having a longer diffusion time than the L_o phase. All experimental systems show a ratio of L_d/L_o autocorrelation amplitudes greater than 1. We expect the L_d autocorrelation to have a greater amplitude than the L_o phase autocorrelation, given equal probe brightness. Varying the simulated probe brightness by a factor of two away from equal is sufficient to reach the cross-over point such that the brighter, faster L_o phase shows a greater autocorrelation amplitude than the slower, dimmer L_d phase (simulated diffusion constants of 0.3 and 0.1 $\mu m^2/sec$ and relative brightness of 2:1 for the L_o and L_d phases, respectively). The converse brightness ratio with the same diffusion constants yields simulated amplitudes in the proper sign but with L_o/L_d autocorrelation amplitudes greater than the majority of the observed experimental data.

While it is difficult to extract an experimental diffusion constant given the complex membrane environment, these data together suggest that the relative brightness of the NR12S probe in the experimental membrane environments is within a factor of 2 of equivalent.

Model systems provide reference spectra for L_o and L_d environments

The sub-diffractive and transitive nature of isolated L_o and L_d regions make collecting *in situ* reference spectra for these domains intractable. Such an experiment would significantly bias the measured spectra towards time-domain-averaged and point-spread-function-blurred of the true spectra of the extreme membrane environments present. Instead we must rely on reference spectra collected in model membrane solutions accepted to produce the desired extrema membrane domain structures. Figure S1 shows these reference spectra for the chosen model domains.

The suitability of these reference spectra for the experimental datasets were evaluated through measuring the resulting error from perturbating these spectra and attempting to fit the experimental data. Spectra for NR12S in reference L_o and L_d are reasonably fit by Gaussian curves. This is clear in the fits of experimental data as well as those appearing

in Reference (*5*). Figure S9A shows data and fits as presented in main manuscript while shows same data and fits with intensities normalized to correct for inhomogeneous spectral bin width. Here the L_o curve has mean = 580.7 nm and σ = 38.8 nm; L_d curve has mean = 615.4 nm, σ = 36.2 nm.

Potential reference spectra were generated from these fits by varying mean values (*i.e.* peak center position) with the other parameters kept constant. Trials were then defined by the peak position of the L_o peak and the distance from there to the L_d peak position (580.7 nm and 34.7 nm in fits, respectively). Representative spectra for each test condition were fit (eq 3) with error defined as cumulative root mean squared distance of the summed filter coefficients from 1.

Results for each test condition shown in S9 C-E with minimum values marked. These minima fall at L_o position/L_o-L_d distance of 585 nm / 35 nm for the Live cell condition, 580 nm /35 nm for the LatB treatment, and 585 nm / 30 nm for the 7KC treatment condition. Each of these values are within 1 bin of the original fit data. Indeed, the bifurcated 'valley' within the data propagating away from the minimum value is further support that the experimental spectra are well-described by this semi-empirical system. Having one or the other domain's spectrum centered near the fit spectrum value produces better fits than having both at more extreme values. The topography of this surface is smooth and demonstrates a continuous approach to an optimum value rather than the chosen spectra carrying critical information not captured by the Gaussian peaks.

The absolute summed rms errors for these minima is 0.2278, 0.2373, or 0.3383 for the control, LatB, and 7KC treatment conditions, respectively. The summed rms error for reference spectra measured in model systems applied to all acquired live-cell experimental spectra is 0.1361 ± 0.0527, 0.1277 ± 0.0395, or 0.2898 ± 0.0504 for the control, LatB, and 7KC treatment conditions (mean ± standard deviation, N = 18, 19, and 10, respectively).

Semi-empirical spectra with positions at or near that derived from spectra of NR12S in the chosen model systems is the best fit for representative experimental data. Errors from using the actual model system spectra are smaller than those from the best-fit semi-empirical result. If a better set of basis spectra existed to fit the experimental data, for example those farther separated than the model system chosen due to more extreme changes in environment, we would expect to see that reflected in the error maps. However, the minimum errors are found using spectra from the model membrane systems. As such we can conclude that the NR12S spectra in the chosen model systems are at or near the optimum basis spectra from which to unmix the signals measured across all of the live cell experiments in this work.

References

1. A. Benda, P. Kapusta, M. Hof, K. Gaus, *Opt. Express* **22**, 2973–2988 (Feb. 2014).
2. M. Wahl, I. Gregor, M. Patting, J. Enderlein, *Opt. Express* **11**, 3583–3591 (Dec. 2003).
3. D. Waithe, M. P. Clausen, E. Sezgin, C. Eggeling, *Bioinformatics*, DOI: 10.1093/bioinformatics/btv687, eprint: http://bioinformatics.oxfordjournals.org/content/early/2015/11/19/bioinformatics.btv687.full.pdf+html (2015).
4. Y. Ma, A. Benda, P. R. Nicovich, K. Gaus, *Biomed. Opt. Express* **7**, 1561–1576 (Apr. 2016).
5. O. A. Kucherak *et al.*, *J. Am. Chem. Soc.* **132**, 4907–4916 (Apr. 2010).

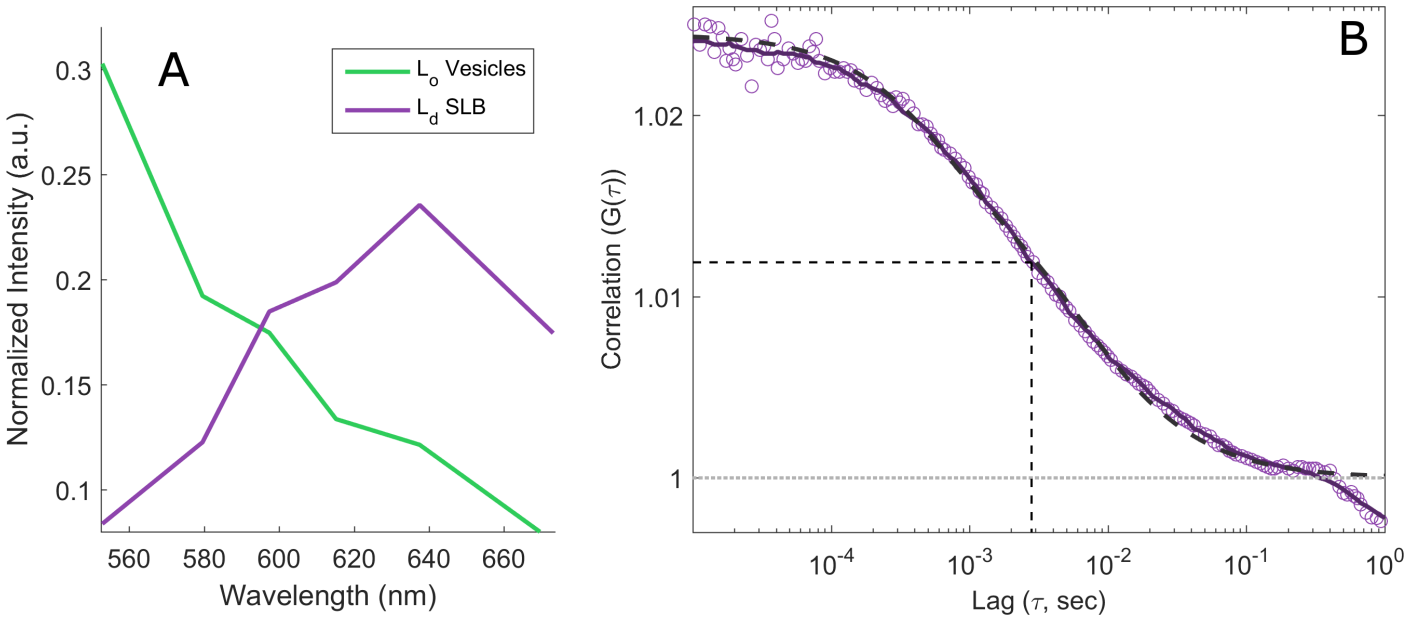

Figure S1: **NR12S in single-phase lipid samples**. A) Spectra of NR12S in single-phase samples. B) Autocorrelation (circles) and smoothed curve (solid line) for NR12S in L_d supported lipid bilayers (D, purple). The $t_{1/2}$ amplitude and time is indicated in each panel as a dashed black line.

Cell Condition	L_o lifetime (mean [95 % CI], ms)	L_d lifetime (mean [% CI], ms)
Control	5.90 [2.93 - 55.52]	14.69 [4.11 - 93.8]
7KC	6.48 [1.97 - 39.70]	24.38 [4.56 - 67.03]
LatB	5.15 [1.80 - 50.27]	13.13 [2.09 - 47.83]

Table S1: **Domain lifetimes by treatment condition.**

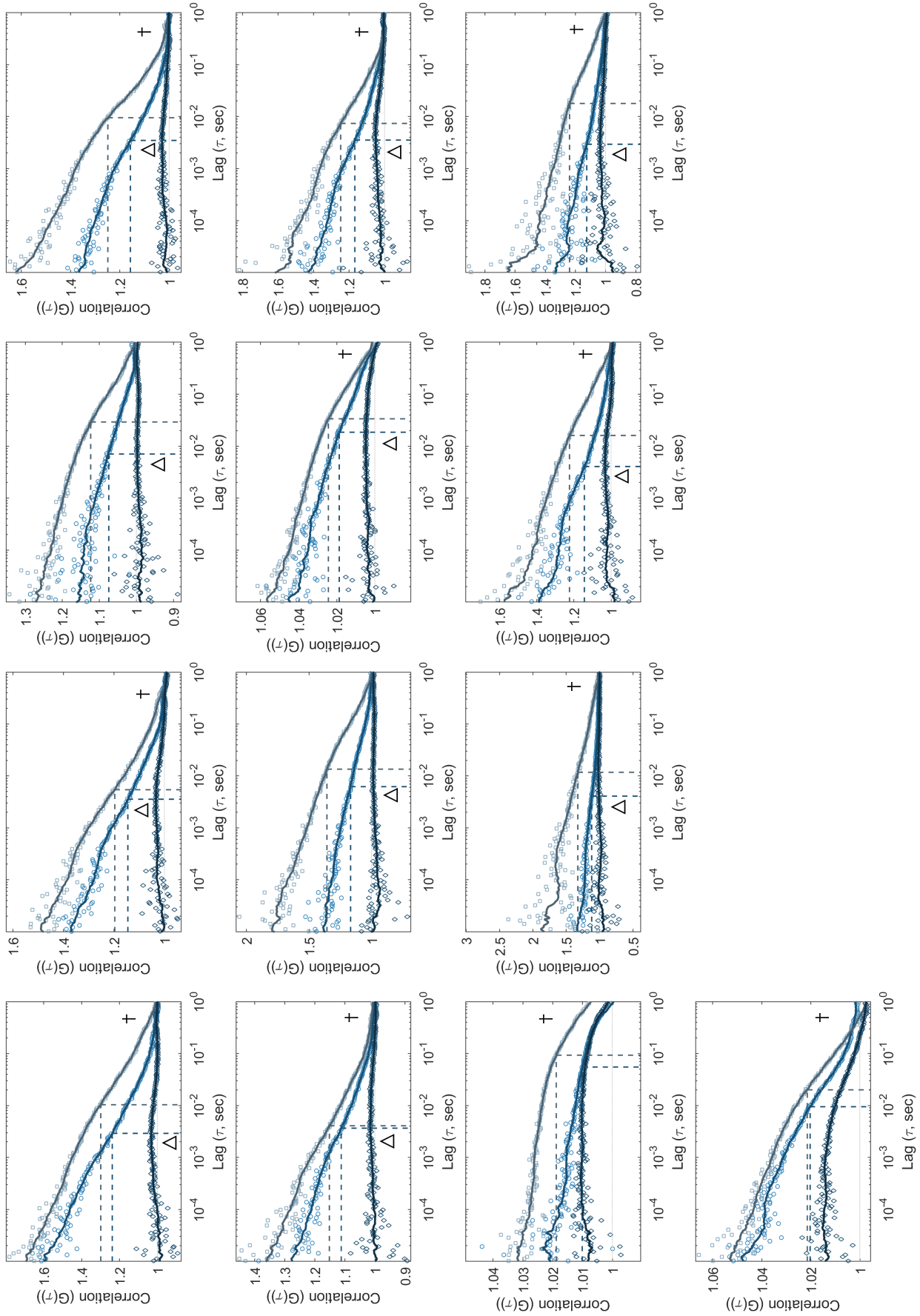

Figure S2: **Correlation results from live COS7 cells stained with NR12S**. Dagger annotations (†) indicate those cross-correlations with positive or negligible cross-correlation signal at $\tau > 10^{-4}$. Triangle annotations (△) indicate those cross-correlations with peaks on the timescale of the autocorrelation decay ($10^{-4} < \tau < 10^{-1}$).

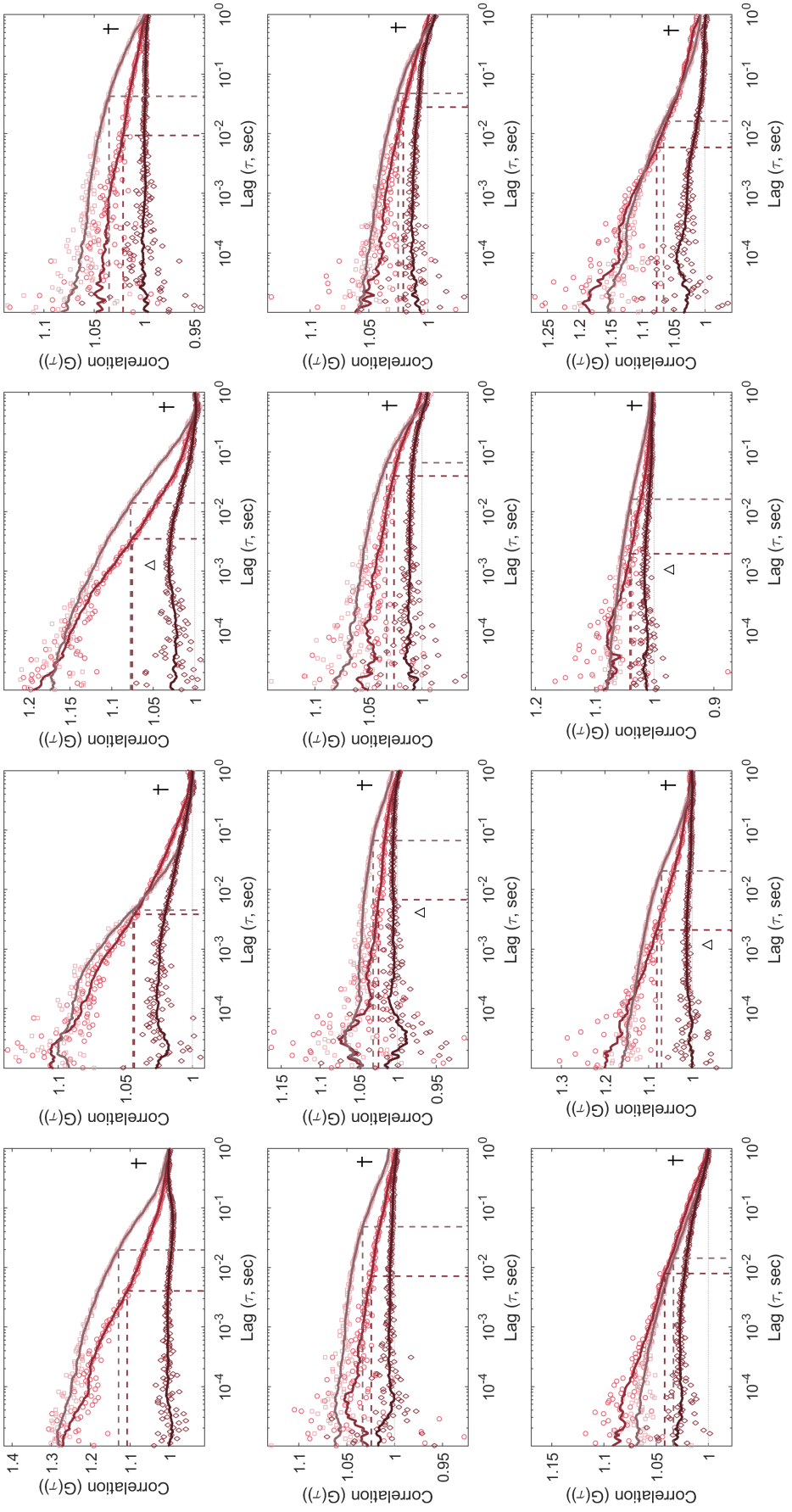

Figure S3: **Correlation results from 7KC-treated cells stained with NR12S**. Dagger annotations (†) indicate those cross-correlations with positive or negligible cross-correlation signal at $\tau > 10^{-4}$. Triangle annotations (△) indicate those cross-correlations with peaks on the timescale of the autocorrelation decay ($10^{-4} < \tau < 10^{-1}$)

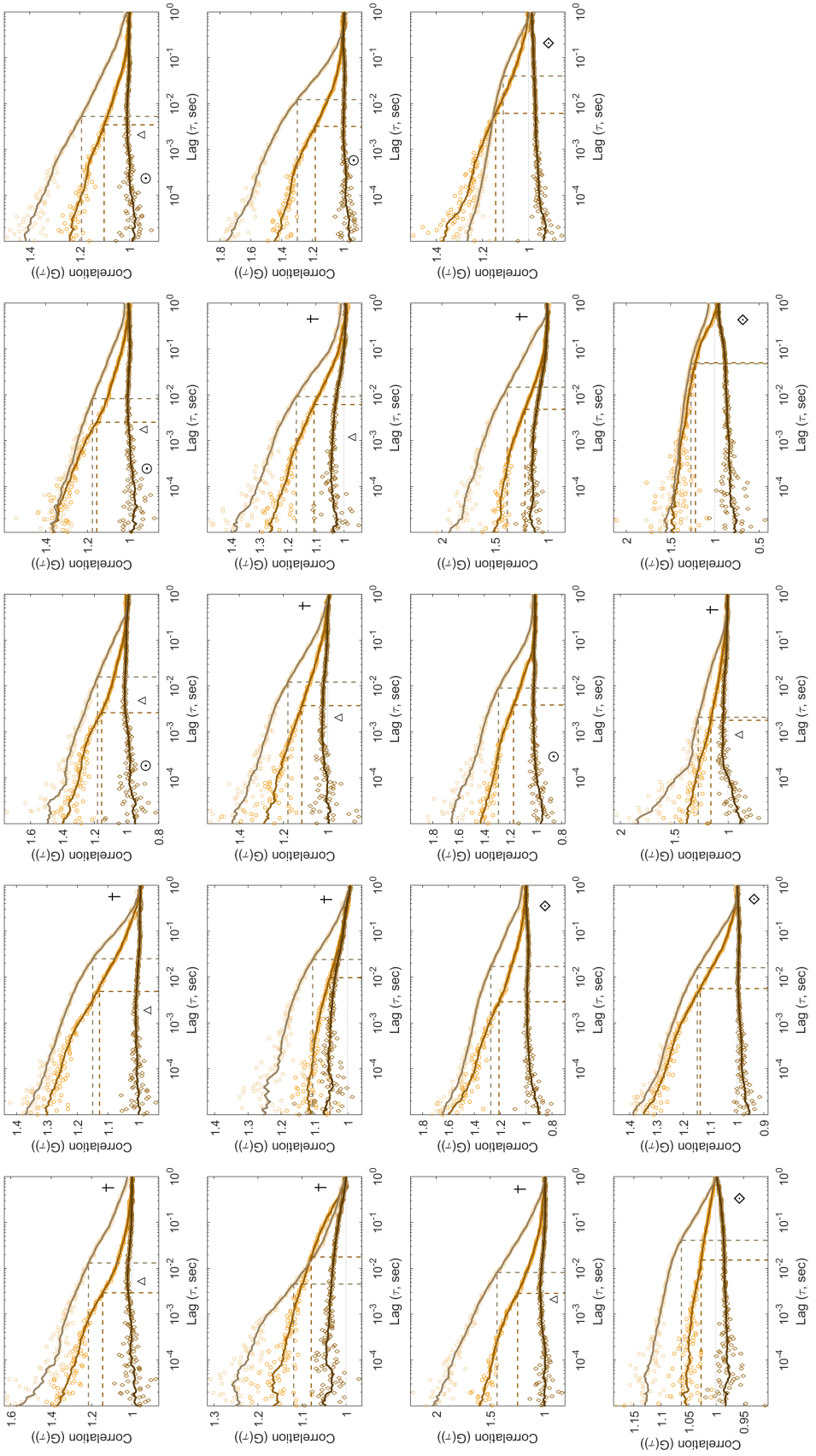

Figure S4: **Correlation results from LatB-treated cells stained with NR12S**. Dagger annotations (†) indicate those cross-correlations with positive or negligible cross-correlation signal at $\tau > 10^{-4}$. Triangle annotations (△) indicate those cross-correlations with peaks on the timescale of the autocorrelation decay ($10^{-4} < \tau < 10^{-1}$). Data sets showing anti-correlations becoming positive at or before the timescale of $\tau < 10^{-4}$ sec are indicated by circle dot annotations (⊙). Those data sets with anti-correlations across $10^{-5} < \tau < 10^{-0}$ timescales are indicated by diamond dot annotations (◈).

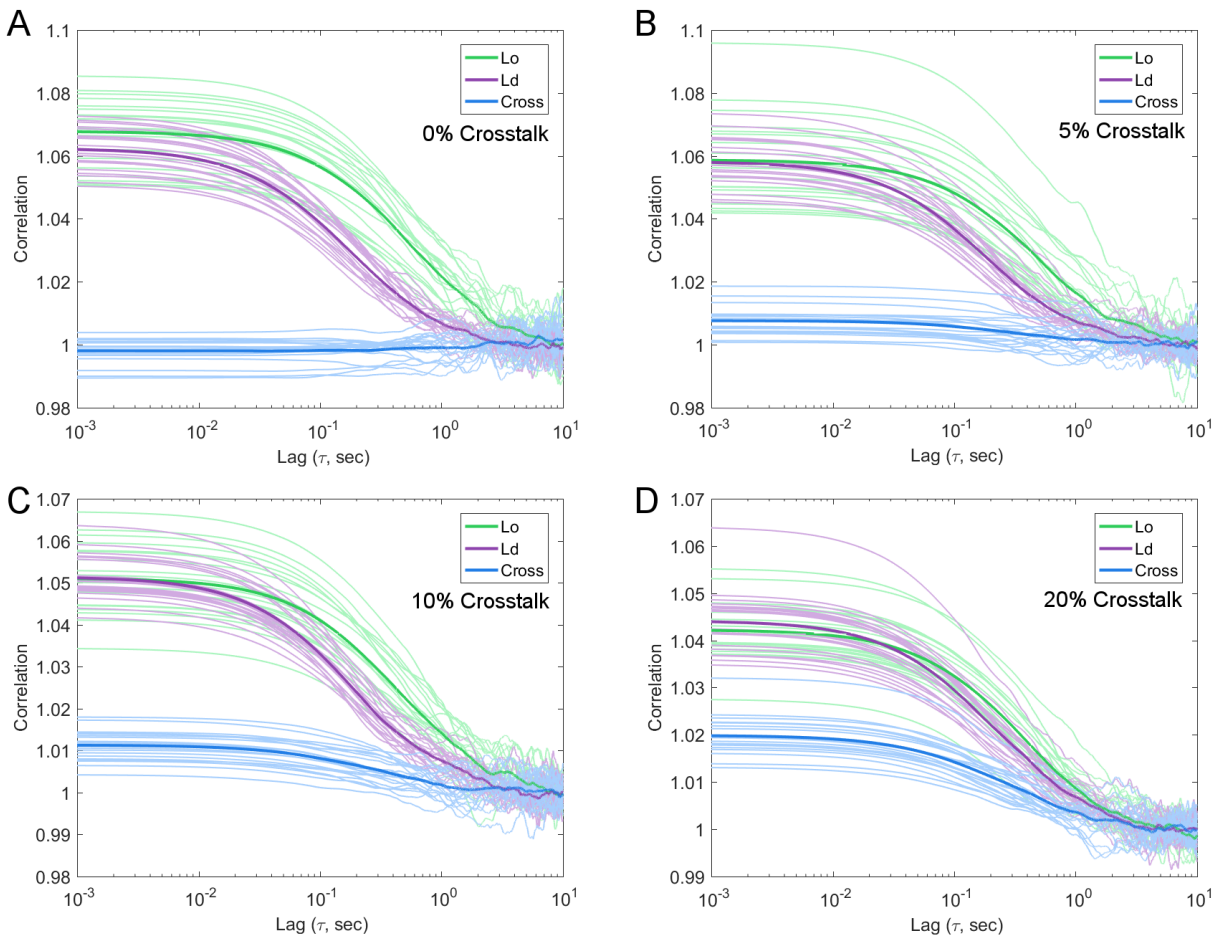

Figure S5: **Results of simulations with increasing amounts of crosstalk.** Simulations were run with probe identity assigned at the beginning of the experiment and retained through the entire run. This identity was assigned as 0 or 1, corresponding to fully L_o or L_d character in trial A. The subsequent trials assigned identity as 0.05 or 0.95 (B), 0.1 or 0.9 (C), or 0.2 or 0.8 (D). Propagating these assignments through to the intensity generation step of the simulation generated the 5%, 10%, or 20% crosstalk indicated. Panels A and D here appear as Figures 2A and 2B in the manuscript. Crosstalk reduces contrast between autocorrelation curves and gives a cross-correlation curve qualitatively similar to the autocorrelation curves.

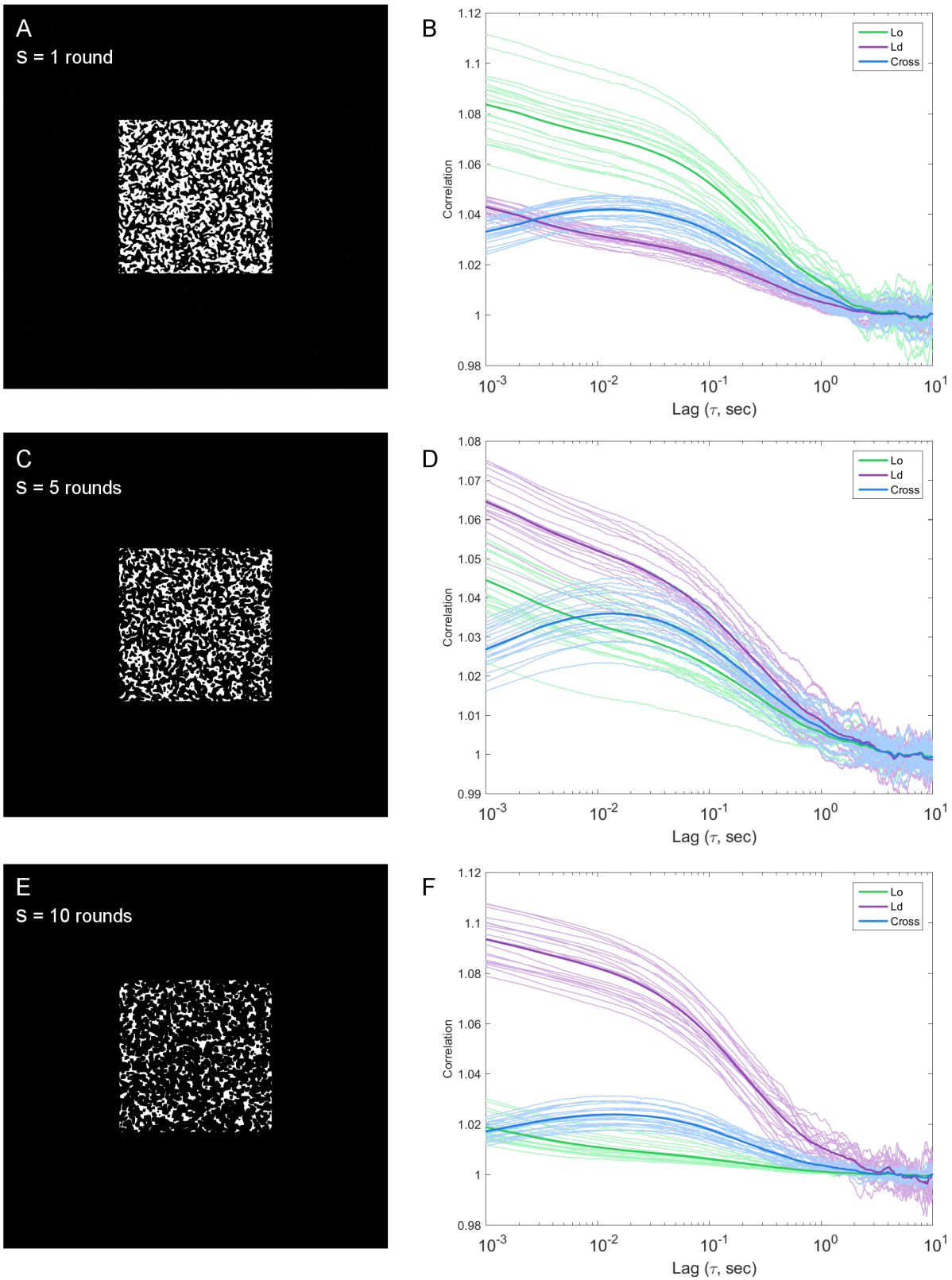

Figure S6: **Results of simulations with varying ratio of domain abundance.** A model membrane favoring one phase abundance over the other was generated by eroding a biphasic lattice of equal phase abundance (equivalent to those in manuscript Figures 2C, 3A, and 4 and SI Figure S7) and performing a morphological erosion operation. The erosion was performed with a square kernel of 3 x 3 pixels; the three conditions vary by how many rounds this erosion was performed. Example generated membranes appear at left with the corresponding correlation results from 20 rounds of probes diffusing in these environments at right. Varying domain abundance retains the qualitative features of the correlation curves though amplitudes of the L_o and L_d autocorrelation curves are altered. Note the amplitude of the cross-correlation curve remains between the two autocorrelation curves.

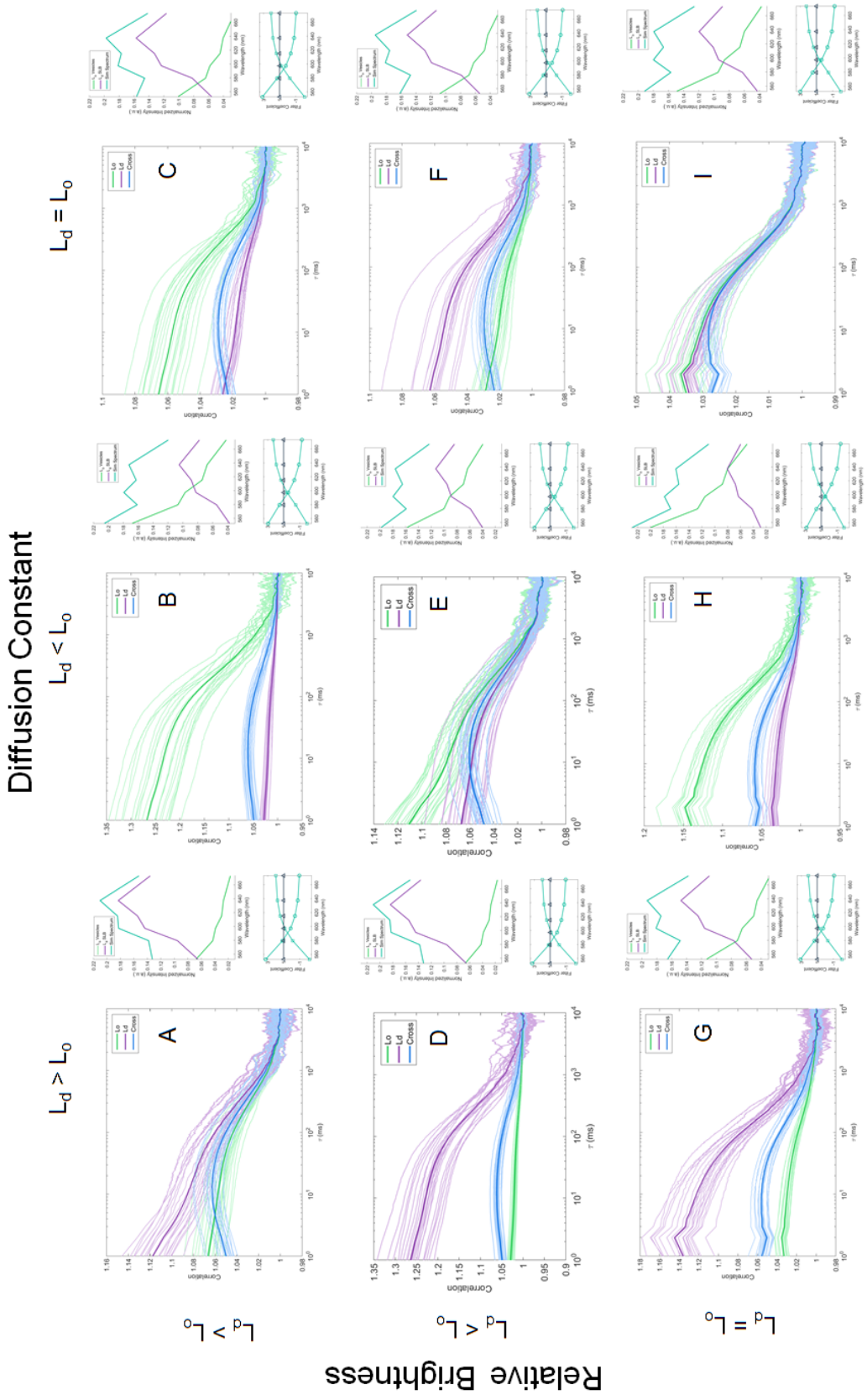

Figure S7: **Results of simulations comparing probe brightness and diffusion constant.** Simulations were run for probes diffusing within a static biphasic membrane lattice (equivalent to manuscript Figure 2 C and D conditions. Diffusion constant was either 0.1 or 0.3 $\mu m^2/sec$. Relative brightness per probe was set to either 1:1 (equivalent), 2:1, or 1:2 for probes in the L_d and L_o phase, respectively. Correlation curves, spectra, and filter coefficients for the 9 condition combinations are shown. The case shown in (G) most closely matches the autocorrelation amplitudes observed in experimental data.

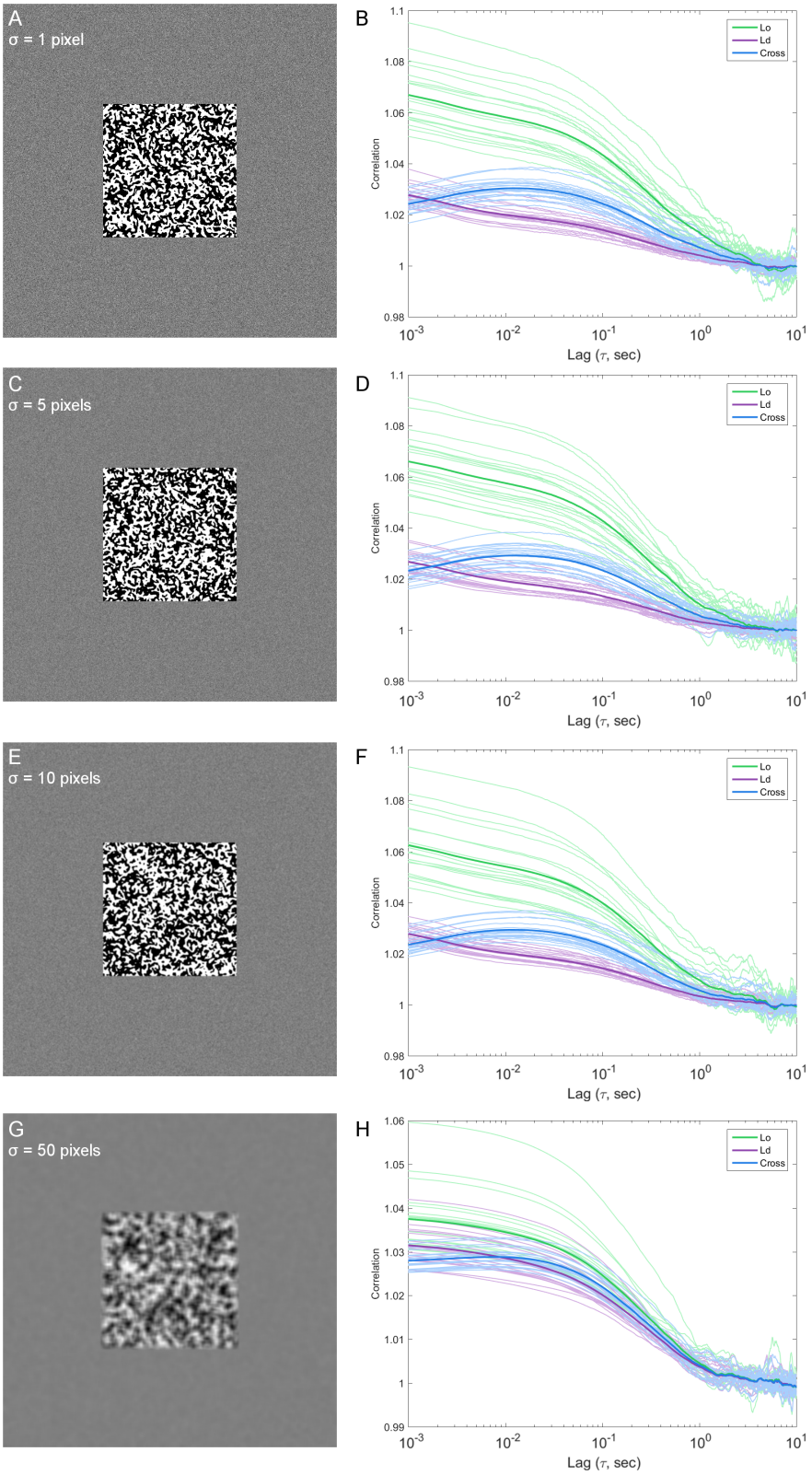

Figure S8: **Results of simulations with varying ratio of domain identity blurring.** A model membrane including gradients between full L_o and L_d character was used in place of a binary biphasic membrane environment; a binary environment appears in manuscript Figures 2C, 3A, and 4 and SI Figures S7 and S6. The gradient membrane was generated by modeling a binary lattice in identical manner to Figure 2C and blurring by a Gaussian kernel of width indicated by σ for each trial. Example modeled environments appear at left with the corresponding correlation results from 20 rounds of probes diffusing in these environments at right. The reduction in contrast between modeled L_o and L_d domains reduces contrast between the correlation curves but does not alter the qualitative features of these curves or their relative amplitudes.

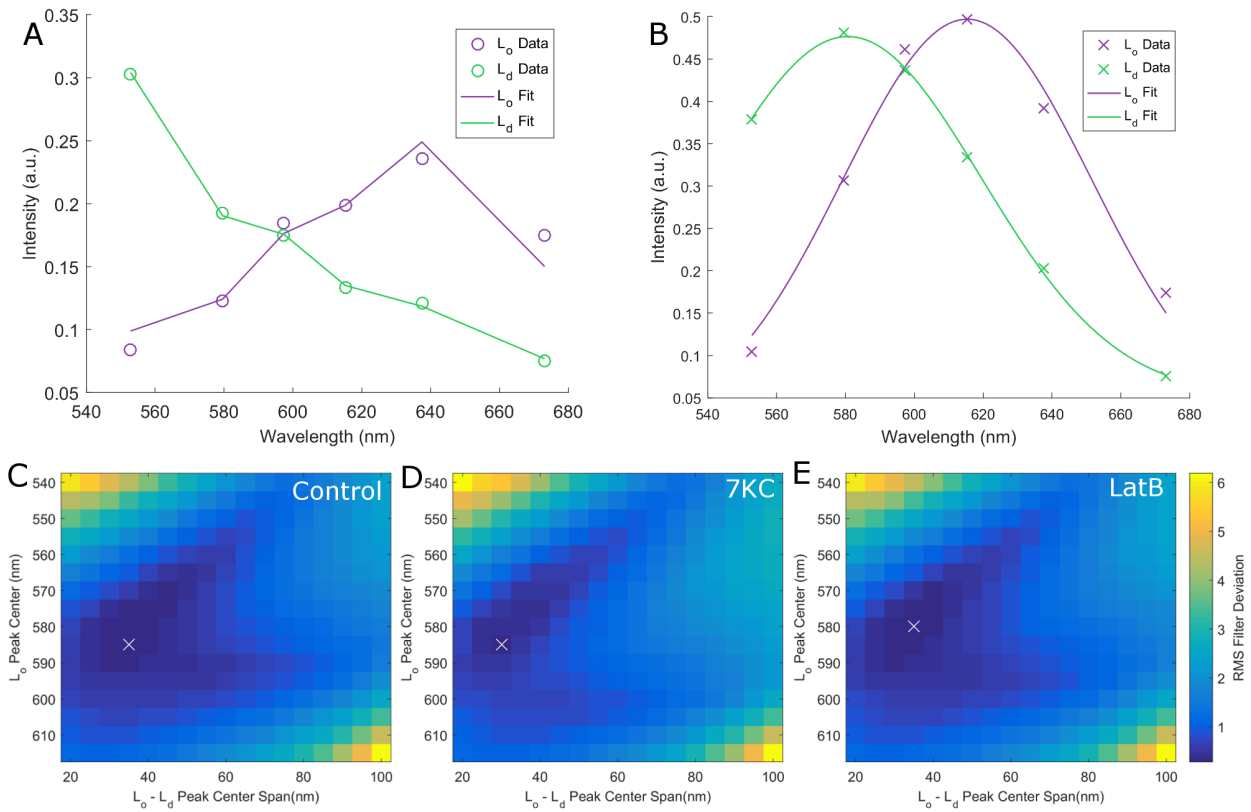

Figure S9: **Results of analysis to determine fitness of chosen basis spectra.** Spectra of NR12S in model membrane systems were fit to Gaussian curves. Panel A shows data as collected and presented in main manuscript; Panel B shows same data as in A but corrected for inhomogeneous spectral bin width of collected spectra. These fit curves were used to fit representative experimental spectra from live cells. Those trials yielding the lowest errors are indicated by white 'x' marks; these fall within 1 bin of the fits to the original experimental spectra.